



Highly dispersed TiO_2 nanocrystals and carbon dots on reduced graphene oxide: Ternary nanocomposites for accelerated photocatalytic water disinfection



Xiangkang Zeng^a, Zhouyou Wang^a, Na Meng^a, David T. McCarthy^b, Ana Deletic^b, Jia-hong Pan^c, Xiwang Zhang^{a,*}

^a Department of Chemical Engineering, Monash University, Clayton, VIC 3800, Australia

^b Environmental and Public Health Microbiology Laboratory (EPHM Lab), Monash Infrastructure Research Institute, Department of Civil Engineering, Monash University, Clayton, VIC 3800, Australia

^c School of Renewable Energy, North China Electric Power University, 2 Beinong Road, Beijing 102206, China

ARTICLE INFO

Article history:

Received 7 June 2016

Received in revised form 30 August 2016

Accepted 4 September 2016

Available online 5 September 2016

Keywords:

TiO_2

Carbon dots

Reduced graphene oxide

Photocatalysis

Disinfection

ABSTRACT

Graphene is widely used as a catalyst support for improved charge separation in TiO_2 photocatalysis. However, the surface oxygen reduction activity of TiO_2 /graphene might be hindered due to the electron storage ability of graphene. In this study, highly dispersed TiO_2 and carbon dots (C-dots) co-decorated reduced graphene oxide (CTR) is synthesized via a simple hydrothermal reaction using TiCl_4 and glucose. Transmission electron microscope, X-ray diffraction, Raman spectroscopy, thermogravimetric analysis and Fourier transform IR spectroscopy are employed to characterize the CTR nanocomposite. The comparison experiment confirmed that C-dots were sourced from the carbonization of glucose. Glucose and TiCl_4 which are mutual dispersants, are critical for forming highly dispersed and uniform-sized C-dots and TiO_2 nanocrystals. With well dispersed TiO_2 and C-dots at separated sites of reduced graphene oxide surface, CTR shows enhanced photocatalytic bacterial inactivation performance under simulated solar light. As confirmed by the reactive oxygen species production, the generation of superoxide anion ($\text{O}_2^{\bullet-}$) and hydrogen peroxide (H_2O_2) is improved. The electrochemical characterization reveals that charge separation in CTR photocatalysis is also promoted. Taken together, the concurrently improved charge separation and surface oxygen reduction activity contribute to an accelerated photocatalytic bacteria inactivation process.

© 2016 Elsevier B.V. All rights reserved.

1. Introduction

Every year millions of people die from diseases caused by pathogens in water [1]. Although a few disinfection technologies have been applied to inactivate pathogens aiming to provide safe drinking water, such as chlorination, ozonation and ultraviolet (UV) irradiation, they are either consume lots of chemicals forming harmful disinfection by-products or energy intensive contributing to global warming [2]. An overarching goal to overturn conventional disinfection methods is to develop some approaches which can affordably and robustly disinfect water from traditional and emerging pathogens, and meanwhile do not create more

problems due to the disinfection processes themselves [3]. As a green approach, photocatalytic disinfection has recently attracted increasing attention. Reactive oxygen species (ROS), which can be generated on a photocatalyst e.g. titanium dioxide (TiO_2) under light irradiation, can effectively inactivate pathogens [4–6]. Most importantly, solar light, the most abundant free renewable energy, can be used as the light source for the photocatalytic system. Thus, TiO_2 photocatalysis presents an economical, effective and environment-friendly oxidation process for disinfection [5,7].

However, the application of TiO_2 for photocatalytic bacterial inactivation is limited in visible light region due to its relatively wide band gap, and high recombination rate of electron–hole pairs [8]. To overcome these challenges, heterostructured photocatalysts have been constructed. With the monolayer structure and superior electron mobility, graphene has been used as a catalyst support to design heterostructured photocatalysts [9]. Combing TiO_2 with graphene not only extends light adsorption, but also

* Corresponding author.

E-mail addresses: xiwang.zhang@monash.edu, zhangxiwang@gmail.com (X. Zhang).

promotes the electron–hole separation because of charge transfer across the TiO_2 –graphene interface [9]. Thus, the photocatalytic activity of TiO_2 –graphene composite is usually much higher compared with bare TiO_2 [9,10]. Apart from light adsorption and electron–hole separation, the surface catalytic reaction is another key step for effective photocatalysis [11]. Unfortunately, the electron storage ability of graphene is low, which hinders the surface oxygen reduction reactions on TiO_2 /graphene composite. It has been demonstrated that if there is no additional electron acceptors on the graphene surface, the electrons from photo-excited TiO_2 can only be partially transferred and stored in the C–C network within graphene [12]. Therefore, if the O_2 molecule is not adsorbed on graphene surface, O_2 reduction with electrons to form ROS will be affected, limiting the photocatalytic activity of TiO_2 /graphene composite. Particularly, the surface oxygen reactions for ROS production are critical to the bactericidal activity of a photocatalyst [7]. Toward the development of high-performance TiO_2 /graphene photocatalysts for disinfection, both highly efficient charge separation and surface oxygen reduction are desirable.

Recently graphene-based ternary photocatalysts such as MoS_2 / TiO_2 /graphene and copper ions/ TiO_2 /graphene were reported and these photocatalysts exhibited superior photocatalytic activity over TiO_2 /graphene [13,14]. With a third co-catalyst on graphene surface, these elaborate works provide a hint to interface TiO_2 and active surface reaction sites on graphene, which concurrently achieve accelerated charge transfer process and improved surface chemical reactions [13,14]. Carbon dots (C-dots) are new carbon nanomaterials with abundant properties such as photo-induced electron transfer, up-conversion and down-conversion photoluminescence, electron reservoir and H_2O_2 decomposition activity [15–17]. Previously, C-dots have been utilised as co-catalysts with TiO_2 to prepare heterostructured photocatalysts [18–20]. Also it has been reported that C-dots are electron donors and show good electrocatalytic activity towards oxygen reduction reactions [21,22]. However, no work has been done to combine C-dots, TiO_2 and graphene together constructing a ternary photocatalyst. Given the photo-induced electron transfer and electron reservoir activities of C-dots [18,21], we hypothesized that TiO_2 and C-dots co-decorated graphene could achieve wide light absorption, efficient charge separation and surface oxygen reaction, which are essential in photocatalytic water disinfection.

In the present study, we report for the first time the synthesis of TiO_2 nanocrystals and C-dots co-decorated reduced graphene oxide (CTR) by a facile method that includes two steps, hydrolysis and hydrothermal reaction. As illustrated in **Scheme 1**, the hydrolysis of titanium tetrachloride (TiCl_4) in GO aqueous suspension containing glucose at low temperature (ice bath) formed amorphous TiO_2 nanoparticles on GO (Fig. S1, Supplementary data). During the hydrothermal reaction, amorphous TiO_2 were crystallized and glucose was converted to C-dots, forming CTR composites. The photocatalytic disinfection experiments revealed that the ternary CTR composites had enhanced performance for bacterial inactivation compared with the binary TiO_2 /reduced graphene oxide (TR) composite. ROS produced by CTR and TR was also probed to explain why improved bacteria inactivation performance was reached. Finally, the possible electron transfer processes for oxygen reduction in TR and CTR photocatalysis were proposed to explore the reaction mechanism.

2. Experimental

2.1. Chemicals

Graphite, TiCl_4 , KMnO_4 , 2, 3-bis (2-methoxy-4-nitro-5-sulfophenyl)-2H-tetrazolium-5-carboxanilide (XTT) sodium salt,

2, 9-dimethyl- 1, 10-phenanthroline (DMP) and terephthalic acid were purchased from Sigma-Aldrich. Other chemicals, including H_2SO_4 , NaNO_3 , H_2O_2 and D-glucose were of analytical grade and purchased from Chem-Supply Australia. Ultrapure water from Milli-Q system was used for all experiments.

2.2. Synthesis

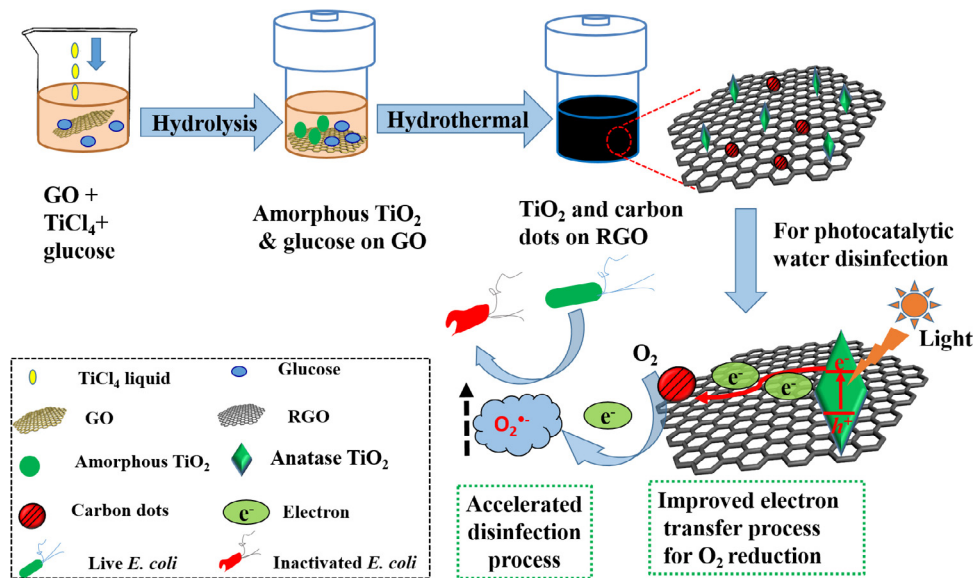
Graphene oxide (GO) was first prepared from graphite flakes using the modified Hummers method [23]. To prepare C-dots/ TiO_2 /rGO (CTR), glucose (1 g) was dissolved in GO colloid suspension (30 ml, 1.5 mg/ml). Then TiCl_4 liquid (75 μl) was then dropwise added to the mixture with vigorous magnetic stirring under ice bath. After 30 min, the grey colloid suspension was transferred into a Teflon-sealed autoclave (50 ml) and maintained at 120 °C for 12 h. The resultant black suspension was filtrated through 0.22 μm filter and washed with DI water twice and finally resuspend in DI water. Additionally, a suspension prepared without glucose using the same procedure was also obtained and termed TiO_2 /rGO (TR) nanocomposite. Sample prepared with GO and the mixture of GO and glucose (pH adjusted to 1.7 by 1 M hydrogen chloride) were treated with the same procedure were termed as rGO and C-dots/rGO respectively.

2.3. Characterization

The morphologies of samples were characterized by scanning electron microscopy (SEM, FEI Nova NanoSEM 450) and transmission electron microscopy (TEM, FEI Tecnai G2 T20 TWIN and FEI Tecnai G2 F20 TWIN). X-ray diffraction (XRD) patterns of samples were collected in the range of 3–80 ° using a Rigaku Miniflex 600 X-ray diffract meter with Cu K α radiation. Fourier transform infrared (FTIR) spectra were recorded with a Perkin-Elmer Frontier FT-IR/FIR Spectrometer. UV-vis diffuse reflectance spectra (DRS) of photocatalysts were analysed by UV-2600 UV-vis Spectrophotometers (Shimadzu). X-ray photoelectron spectroscopy (XPS) analysis was performed using an AXIS Ultra DLD spectrometer (Kratos Analytical Inc., Manchester, UK) with a monochromated Al K α source at a power of 180 W (15 kV \times 12 mA). Thermogravimetric analyses (TGA) were conducted on a Pyris Diamond TG/DTA (PerkinElmer) apparatus at a heating rate of 10 °C min $^{-1}$ (40–800 °C in air flow). The particles size distribution of CTR and TR suspension were analysed with an AccuSizer 780 particles sizing system (Particle Sizing Systems, Inc. Santa Barbara, Calif., USA).

2.4. Photocatalytic water disinfection

The photocatalytic disinfection activity of each sample was evaluated in terms of the inactivation of *Escherichia coli* (*E. coli* ATCC 11775). To obtain our inoculum, a single colony was placed in 10 ml Luria Bertani (LB) medium at 37 °C in a shaking water bath, overnight. 0.2 ml of this solution was then transferred to 10 ml LB medium and incubated until it reached an optical density of 0.5 at 600 nm. The cells in the media were harvested by centrifugation, washed twice and then diluted with sterile phosphate buffer (PB 0.1 M, pH 7.0) to 1.5×10^3 colony forming units/ml (CFU/ml). For the photocatalytic disinfection process, 3 mg of the photocatalyst was added to 30 ml of the *E. coli* suspension buffer and stirred at 300 rpm for 10 mins before light irradiation (non-irradiated controls were kept in the dark). A 300 W Xe lamp (Newport) with AM 1.5 air filter was used as a simulated solar light source. At the given time intervals (i.e. 0, 15, 30, 45 and 60 mins), aliquots were taken from the suspension buffer and remained at 4 °C for no more than 2 h before plating. 0.1 ml of the suspension (undiluted, three replicates) was spread onto LB agar plates and incubated at 37 °C for 18 h to form viable colony units. The bacterial inactivation rate was



Scheme 1. Illustration of the synthesis of CTR nanocomposite and its application for photocatalytic water disinfection.

calculated as $\log (N/N_0)$ where N and N_0 are the bacterial concentration of samples taken at certain time and before light irradiation respectively.

For TEM images of *E. coli* cells, 5 ml of *E. coli* suspension (10^8 CFU/ml) were mixed with 2 mg of the photocatalyst and treated with light irradiation for 60 mins. The suspension was then centrifuged for 10 min at 8000 rpm, the pellets were collected together with the catalyst. Untreated *E. coli* were also collected and used as a control. The pellets were then treated by a serial of steps for imaging as described in detail in our previous work [24].

2.5. Measurement of reactive oxygen species

The photocatalytic generation of reactive oxygen species was measured in the same PB buffer solution containing the same amount of photocatalyst except without *E. coli* cells. $\text{O}_2^{\bullet-}$ was measured with 0.1 mM XTT and the formed XTT-formazan was measured by absorbance at 470 nm [25]. H_2O_2 was determined by a colorimetric method using copper (II) ions and DMP at 454 nm [26]. $\bullet\text{OH}$ was detected with the terephthalic acid solution using the fluorescence technique [27]. During photocatalytic process, 3 ml of suspension was taken at certain irradiated time and filtered through a $0.22 \mu\text{m}$ Millipore filter to remove the photocatalysts. The filtrated were analysed by UV-2600 UV-vis Spectrophotometers (Shimadzu) or F-7000 fluorescence spectrophotometer (Hitachi) for absorbance or fluorescence measurement.

2.6. Electrochemical experiments

Electrochemical experiments were performed in a three-electrode cell on a CHI 660E workstation. To prepare the working electrodes, 10 μl of photocatalyst-ethanol ink (1 mg/ml) was loaded onto a glassy carbon electrode of 3 mm in diameter. After drying at room temperature, 5 μl of 5 wt% Nafion solution was added to paste the slurry. The resultant electrode served as the working electrode, with a platinum wire as the counter electrode and an Ag/AgCl (saturated KCl) electrode as the reference electrode. Current-potential curves were measured in 0.1 M phosphate buffer (pH 7.0) electrolyte solution. Electrochemical impedance spectra (EIS) were measured in the same electrolyte by applying 5 mV alternative signal versus the reference electrode over the frequency range of 1 MHz to 0.1 Hz. Prior to and during all measurements,

the electrolyte solution was purged with high-purity N_2 or O_2 gas. Photocurrents were measured in the same three-electrode system. The light was produced by a 300 W Xe lamp (Newport) with AM 1.5 air filter. Transient photocurrent responses for the electrodes were measured under 0.6 V bias vs Ag/AgCl in 0.5 M Na_2SO_4 solution.

3. Results and discussion

3.1. Preparation and characterization of catalyst

TEM images (Fig. 1a and b) of CTR show highly dispersed particles (around 10 nm) deposited on the surface of rGO sheet. The high-resolution TEM (HRTEM) images of CTR (Fig. 1c and d) indicate both TiO_2 nanocrystals and C-dots exist on rGO surface. The lattice fringe spacing of 0.35 nm (Fig. 1c) is assigned to anatase (101) facet of TiO_2 [28]. While the nanocrystals with lattice fringe spacing of 0.32 nm and 0.21 nm (Fig. 1d) are corresponding to the (002) and in-plane (100) facet of disordered graphitic carbon, respectively [20,29]. To further prove the co-existence of TiO_2 and C-dots, energy-dispersive X-ray spectroscopy (EDX) mapping was done (Fig. 1e and f). The Ti element mapping image (Fig. 1f) demonstrates a good distribution of TiO_2 on the rGO. As both C-dots and rGO sheet are carbon materials, C-dots were not clearly seen in the C element mapping image (Fig. 1g). But as shown in EDX spectra (Fig. S2), there are only three elements, C, Ti and O, in the nanocomposite. By comparing Fig. 1e and f, it can be found that some nanoparticles marked by yellow circles do not display a signal of titanium, indicating that they must be C-dots.

Both TR and CTR are black samples and show good light absorption in the visible light according to the UV-vis diffuse reflectance spectra (Fig. S3). Fig. 2a reveals the X-ray diffraction (XRD) patterns of graphene oxide (GO), reduced graphene oxide (rGO), TR and CTR nanocomposites. Notably, TiO_2 in TR and CTR crystallized in an anatase phase structure (JCPDS No. 21-1272). Moreover, after the hydrothermal reaction, the typical diffraction peak of GO (9.8°) shifted to around 24°, which reveals a graphitic structure of rGO, suggesting the reduction of GO [30]. For CTR and TR, this peak shifts to around 15° due to the presence of nanoparticles on rGO surface which enlarge the interlayer spacing [31]. According to previous studies, C-dots show typical peaks at around $2\Theta = 20^\circ$ in the XRD pattern [32]. However, when comparing the patterns of TR and CTR, no peaks associated with C-dots were detected. The reason

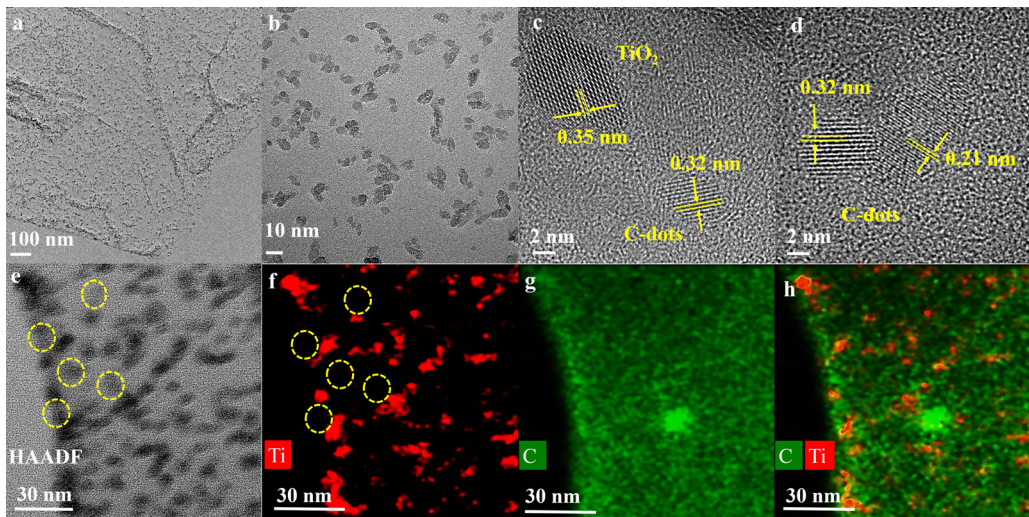


Fig. 1. TEM (a and b) and HRTEM(c and d) images of CTR. (e and f) EDX elemental mapping of Ti and C in CTR.

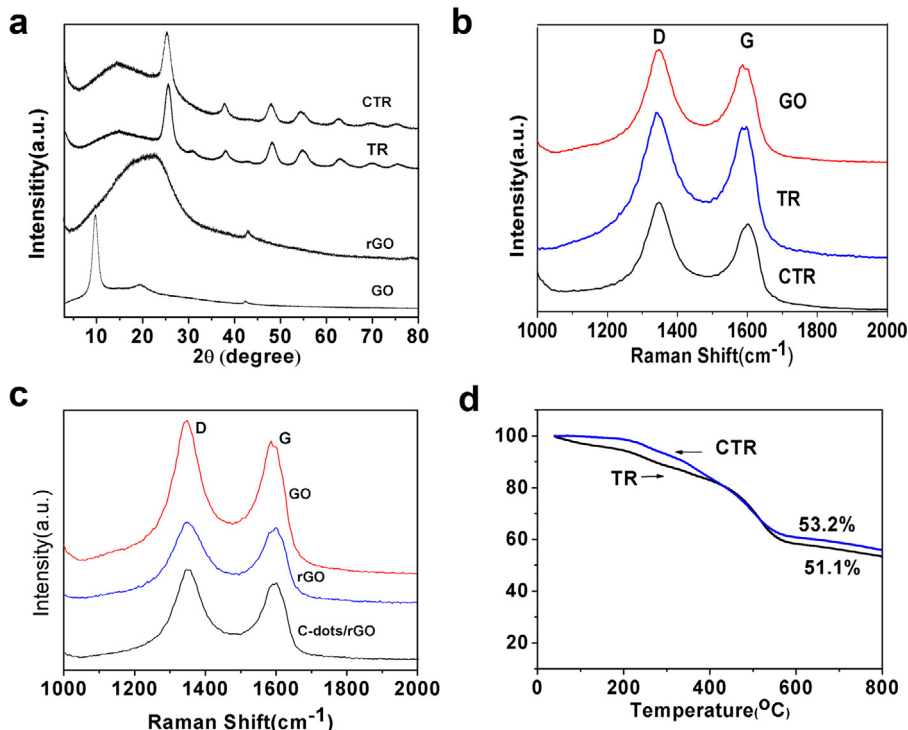


Fig. 2. (a) XRD patterns of GO, rGO, TR and CTR nanocomposites; (b and c) Raman spectra of GO, TR, CTR, rGO and C-dots/rGO; (d) TGA curve obtained for the CTR and TR under air atmosphere.

could be that the content of C-dots in CTR was not enough to be detectable by XRD. Further evidence for the existence of C-dots in CTR comes from X-ray photoelectron spectra (XPS). The C1s spectra of rGO, C-dots/rGO, TR and CTR shows that the successful reduction of GO via the hydrothermal process, verified by the diminished C=O, C=O, and O—C—O groups intensity (Fig. S4 & Table S1). Furthermore, as C-dots have oxygen groups, it is worth noting that the C=O and O—C—O groups intensity in C-dots/rGO is relative higher than that of rGO due to the deposition of C-dots on rGO. Similarly, the C=O and O—C—O groups intensity in CTR is also higher than that of TR, further implying the existence of C-dots on rGO in CTR. Raman spectra provide some addition insights into the structure information of the nanocomposites. Fig. 2b–c reveals the characteristic D (1348 cm^{-1}) and G (1598 cm^{-1}) bands of graphene in the

hybrid. The intensity ratio (I_D/I_G) for the D and G band of TR was lower than that of GO (1.10 vs 1.15), suggesting fewer defects of rGO after hydrothermal reaction [33,34]. Compared with TR, CTR does not exhibit obvious new peaks or shifts, proving C-dots could have similar graphitic D band (corresponding to the vibrations of carbon atoms with dangling bonds in the disordered carbon structure or vacancy defects in C-dots) and G band (arising from the vibration of the sp²-bonded C atoms in the graphene-related materials) [35]. But, the I_D/I_G ratio of CTR increased compared with that of TR (1.18 vs 1.15). The same result was also found when comparing rGO and C-dots/rGO (Fig. 2c). It is known that C-dots contain sp³ hybrid carbon and oxygen groups. These groups of C-dots may cause defects when it was deposited on rGO, therefore, the I_D/I_G ratio increased [33]. The difference of I_D/I_G ratio between TR and

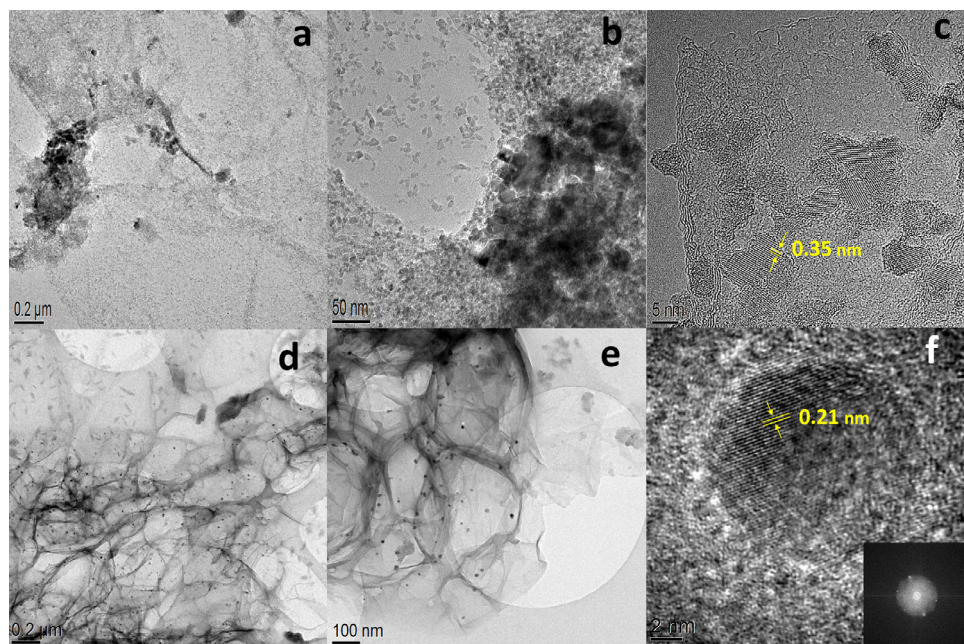


Fig. 3. TEM (a and b) and HRTEM (c) images of the TiO_2 /reduced graphene oxide (TR) composite prepared without glucose. (d and e) TEM and HRTEM (f) images of C-dots/reduced graphene oxide (C-dots/rGO) composite prepared without TiCl_4 . Inset (f) is the corresponding 2D fast Fourier transform (FFT) pattern, exhibiting the hexagonal crystalline structure of the C-dots.

CTR further proves the presence of C-dots in CTR. To determine the content of TiO_2 in TR and CTR composite, thermalgravim analysis (TGA) were conducted. Fig. 2d shows that the contents of TiO_2 in TR and CTR are almost the same, being 51% and 53% respectively. It is assumed that TiCl_4 is completely converted to TiO_2 and the mass of GO does not change after the hydrothermal process. According to the amount of precursors (TiCl_4 and GO), the theoretical mass ratio of TiO_2 /rGO in CTR is 1.22/1. Therefore, the mass ratio of rGO and C-dots in CTR nanocomposite is calculated to be 43.4% and 3.6% respectively.

To further investigate the role of glucose in the synthesis of CTR, we first investigated the morphology of TR (the composite prepared without glucose). The TEM images of TR (Fig. 3a–c) show TiO_2 particles are prone to aggregate on the rGO surface. By increasing the concentration of glucose from 0 to 33 mg/L, the dispersion of TiO_2 nanoparticles on rGO was improved (Fig. S5). It can be explained that due to the abundant hydroxyl groups, glucose molecules surround TiO_2 and then control the growth of TiO_2 nanocrystals on graphene and prevent the aggregation [28,36]. This leads to the formation of well-dispersed TiO_2 nanocrystals on the rGO nanosheets.

To reveal whether C-dots are sourced from glucose, hydrothermal treatment of GO suspension alone without glucose was conducted under the same conditions. No carbon dots were found on resultant rGO (Fig. S6 and S7). This indicates that C-dots of CTR composite are likely sourced from glucose. However, the hydrothermal carbonization of glucose to form C-dots usually requires a reaction temperature at, or above, 180°C [37,38]. The reaction temperature in the present study was only at 120°C to prevent the damage of rGO at high temperature, but the crystallization of glucose was still observed. We noticed that the pH of GO aqueous suspension was around 3.3, and after dropwise adding TiCl_4 to GO aqueous suspension in CTR synthesis the pH of the solution dropped further to 1.7 due to the formed hydrochloric acid from the hydrolysis of TiCl_4 . To investigate the effect of pH on the carbonization of glucose, a glucose aqueous solution was adjusted to pH = 1.7 with hydrochloric acid and then underwent a hydrothermal treatment at 120°C . We found that small crystallized carbon dots were formed (Fig. S8c and d). In contrast, no carbon dots were formed in the

control glucose solution without addition of hydrochloric acid (Fig. S8a and b). Similarly, small particles on rGO was also found when the mixture of GO and glucose was treated at pH = 1.7 (Fig. 3d and e). And its HRTEM image (Fig. 3f) shows these particles are crystallized carbon dots. Therefore, it can be concluded that C-dots are formed by the hydrothermal carbonization of glucose, rather than GO. This also indicates that hydronium ion from hydrochloric acid may act as a catalyst in the dehydration and decomposition of glucose [32], which promotes the forming of carbon dots from glucose at a relatively low temperature during the hydrothermal reaction.

Interestingly, when there was no TiCl_4 in the mixture, the sizes of C-dots are not uniform (Figs. 3d and e and Fig. S8). A previous study reported that during the hydrothermal carbonization of glucose, inorganic salt such as monopotassium phosphate can prevent carbon nuclei from growing and assembling into large carbon particles [37]. Therefore, the formation of uniform and small C-dots in the CTR nanocomposite could be attributed by the inorganic salt TiCl_4 . This result suggests TiCl_4 and glucose are mutual dispersants for in-situ growth of uniform TiO_2 nanoparticles and C-dots on rGO sheet. Moreover, in the absence of TiCl_4 , hydrogel, rather than dispersed suspension, was formed in the hydrothermal treatment of GO suspension regardless of adding glucose (Fig. S6). This indicates that the amorphous TiO_2 nanoparticles on graphene formed in the hydrolysis step can act as spacers to prevent the stacking of exfoliated GO nanosheets during the hydrothermal reaction.

Despite both TR and CTR particles form suspensions in water, it is worth noting that their sizes are quite different. As shown in Fig. 4a and b, CTR nanocomposites forms a stable suspension while the TR particles trend to aggregate together to form big particles. The particle sizing analysis reveals that the mean size of CTR in water is $1.20\text{ }\mu\text{m}$ while that of TR is $7.44\text{ }\mu\text{m}$ (Fig. S9). Fourier transform infrared spectroscopy (FTIR) shows that more oxygen-containing groups exist in CTR due to C-dots in the composite, (Fig. S10), which is in good agreement with the result from XPS spectra. These hydrophilic oxygen groups ($\text{C}=\text{O}$ and $\text{O}-\text{C}-\text{O}$) might lead to the high dispersibility of CTR in water.

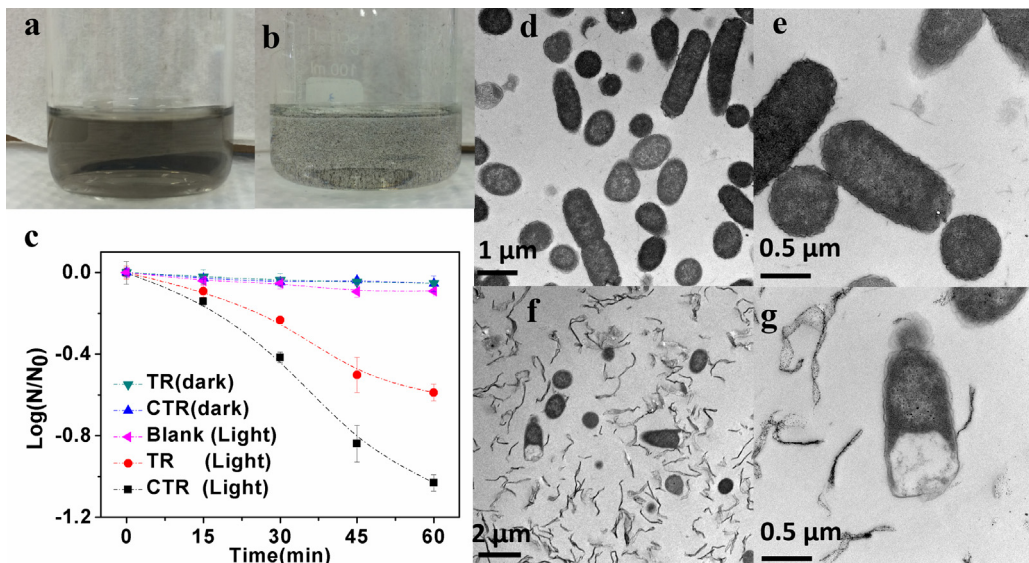


Fig. 4. CTR (a) and TR (b) suspension in water; (c) *E. coli* inactivation by TR and CTR composite; (d-e) TEM images of untreated *E. coli* cells (control); (f-g) TEM images of *E. coli* cells treated by CTR under simulated solar light.

3.2. Photocatalytic water disinfection

We investigated the photocatalytic activity of the TR and CTR towards inactivating *Escherichia coli* (*E. coli*) in aqueous phosphate-buffered (PB, 0.1 M, pH 7.0) solution under simulated solar light. *E. coli* inactivation performance of the TR and CTR composites are illustrated in Fig. 4c. Under dark or simulated solar light irradiation, few *E. coli* are inactivated. When the photocatalysts were irradiated by light, CTR slurry system reached 1.03 log inactivation of *E. coli* in 60 mins but only 0.58 log inactivation by TR. These results show that the photocatalytic inactivation activity of CTR composite is improved by C-dots. To better understand the destruction of *E. coli* cells in the CTR system, the microstructure and morphology of *E. coli* cells before and after photocatalytic inactivation were identified by TEM. Fig. 4d and e show representative TEM images of untreated *E. coli* cells, which show uniform electron density, suggesting their membrane and wall structures are intact and well-preserved. After photocatalytic inactivation, a portion of the *E. coli* cell structure disappeared, indicating damage to the membrane and leakage of interior components (Fig. 4f and g) [39]. It has been known that rGO nanosheet can inactivate *E. coli* cell through membrane and oxidative stress when they are directly contacted [40]. However, in this study, rGO should not be the main disinfectant, as only few cells are inactivated when *E. coli* cells were incubated with TR and CTR nanocomposite under dark conditions. In photocatalytic reactions, electrons and holes generated from photo-excited TiO₂ react with O₂ and H₂O forming ROS, such as superoxide radicals (O₂^{•-}), hydrogen peroxide (H₂O₂) and hydroxyl radicals (•OH). These ROS diffuse into the solution and attack the cells around the photocatalyst, causing alterations of cell permeability and/or even decomposition of the cell wall [7,41].

3.3. Photocatalytic generation of ROS

To identify the role of C-dots in the enhancement of photocatalytic disinfection efficiency, the photocatalytically generated ROS in TR and CTR slurry systems were probed. Firstly, O₂^{•-} was probed by the widely used 2,3-Bis (2-methoxy-4-nitro-5-sulphophenyl)-2H-tetrazolium-5-carboxanilide (XTT). O₂^{•-} reduces XTT to form XTT-formazan and the specific absorption peak at 470 nm of XTT-formazan can be used to quantify the amount of O₂^{•-} [25]. As shown in Fig. 5a, the concentration of the produced XTT-formazan in CTR

system is much higher than that in TR, indicates that O₂^{•-} in the former system is higher than that in the latter. Given a significant enhancement for O₂^{•-} production, it can be concluded that the O₂ reduction activity is boosted by C-dots in the CTR slurry. Moreover, significantly more H₂O₂ was generated by CTR than TR (Fig. 5b). Interestingly, the amount of •OH in CTR is less than that in TR (Fig. 5c).

Generally in a TiO₂ photocatalytic aerobic oxidation process, oxygen molecules are reduced by a series of sequential single-electron reduction reactions and concomitantly various reactive oxygen species are formed [42]. The first single-electron reduction reaction produces O₂^{•-} when O₂ accepts one electron from the TiO₂ conduction band (Eq. (S2)). And H₂O₂ comes from either O₂^{•-} when O₂^{•-} accepts one electron with proton in the solution (pH<4.8) (Eq. (S3–S5)), or •OH when two •OH combines (Eq. (S6 and S7)) [42]. As the pH of the buffered solution used in this study is 7.0, H₂O₂ should mainly come from the combination of •OH. To prove this, 2-propanol (holes scavenger) was added to the solution. As 2-propanol is an efficient holes scavenger, the forming of •OH will be limited with 2-propanol in solution [43]. If H₂O₂ comes from •OH, consequently the production of H₂O₂ should also be reduced in the presence of 2-propanol in solution. As shown in Fig. S11, the concentration of H₂O₂ in the solution in the presence of 2-propanol was significantly lower than that in the absence of 2-propanol. Therefore, this result indicates that H₂O₂ is mainly formed through the combination of •OH in the TR and CTR systems. It can also explain why CTR system has higher concentration of H₂O₂, but lower concentration of •OH compared to TR system. The results indicate that C-dots facilitates the conversion of •OH to H₂O₂.

Although it is well known that •OH has higher oxidizing power than H₂O₂ and O₂^{•-}, CTR has better photocatalytic disinfection performance than TR. This can be explained by the difference in the lifetimes of these ROS, which determine the distance they can diffuse in aqueous solutions. The lifetime of •OH is the shortest, being less than 10 ns in cells [44]. Therefore, it can only diffuse a very short distance (less than 20 nm) and attack the *E. coli* cells very close to the surface of catalyst [7,45]. In contrast, O₂^{•-} and H₂O₂ can diffuse over long distances due to their longer lifetimes [45], making it possible to contact with the *E. coli* cells which are far from the photocatalyst in aqueous solution. When contacted with *E. coli* cells, as confirmed by the TEM images (Fig. 4f and g), long-lifetime O₂^{•-} and H₂O₂ will damage the cell permeability and/or even decom-

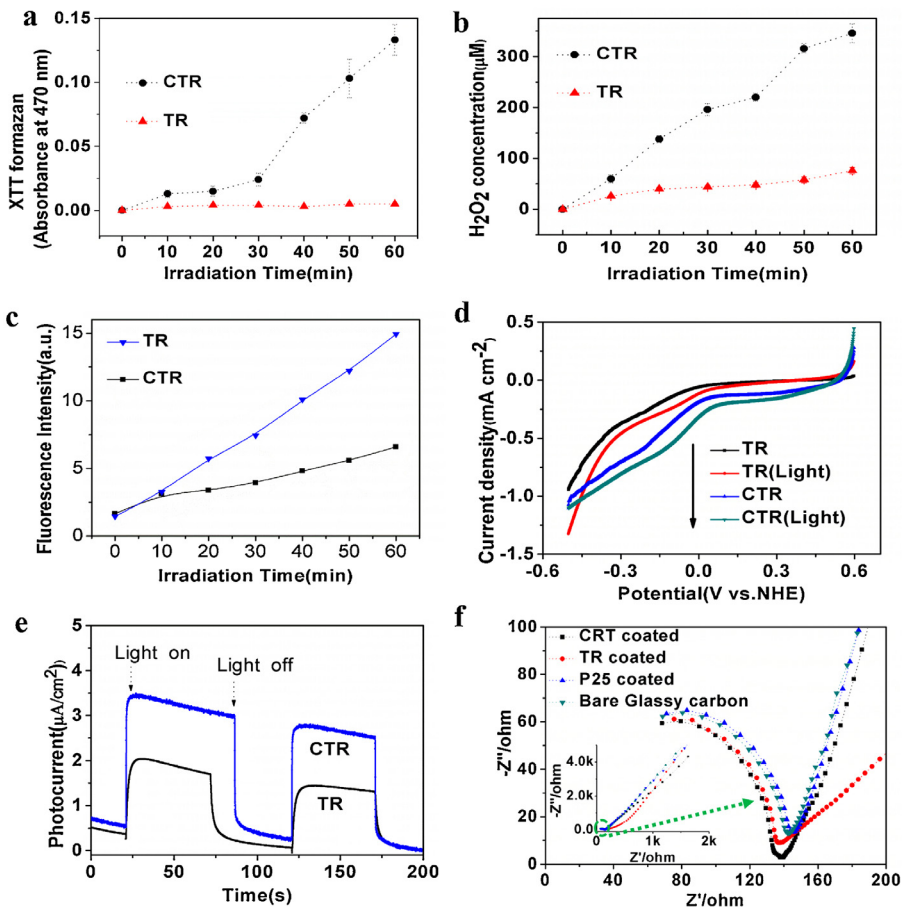


Fig. 5. Photocatalytic generation of $\text{O}_2^{\bullet-}$ (a), H_2O_2 (b) and $\bullet\text{OH}$ (c) by TR and CTR under simulated solar light; (d) Electrochemical current-potential curves of the prepared electrode in O_2 -saturated PB buffer solutions with and without light. (e) Photocurrent curve of TR and CTR; (f) EIS Nyquist plots of the prepared electrodes in O_2 -saturated PB buffer solutions.

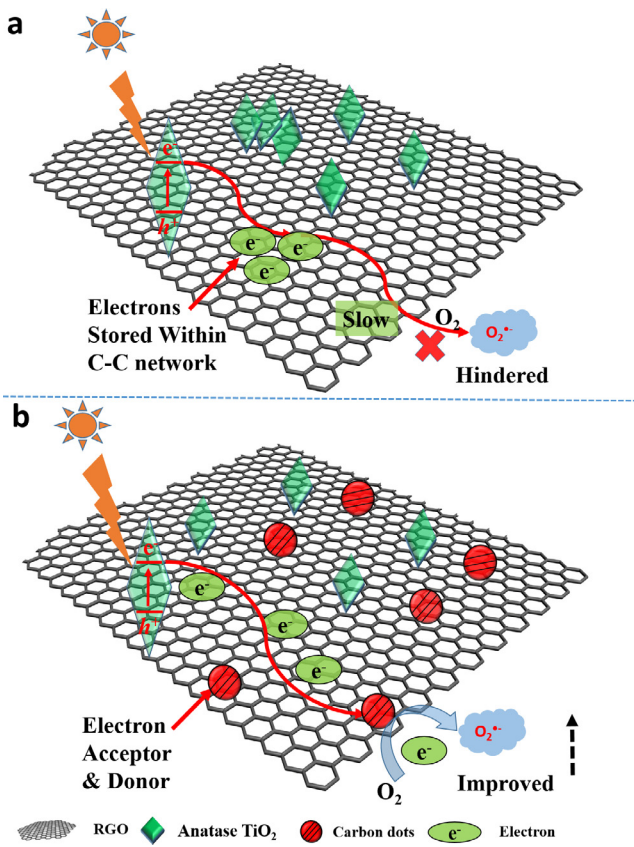
position of the cell wall, thus inactivating the *E. coli* cells [7,41]. This suggests that relatively long-lived species ($\text{O}_2^{\bullet-}$ and H_2O_2) are more crucial than the short-lived $\bullet\text{OH}$ for bacteria inactivation. Therefore, due to higher concentration of $\text{O}_2^{\bullet-}$ and H_2O_2 , CTR still achieved better disinfection performance than TR did even though the concentration of $\bullet\text{OH}$ in CTR is relatively lower.

3.4. Improved electron transfer for O_2 reduction

To further examine the O_2 reduction process, electrochemical O_2 reduction was investigated on the film electrode prepared by CTR and TR, respectively. When the electrode was in a solution purged with nitrogen gas, little current was observed (Fig. S12). While in O_2 saturated solution, an obvious reduction current was observed, indicating that O_2 reduction occurred on the composite electrodes. As indicated by Fig. 5d, a higher O_2 reduction current is observed on CTR electrode over TR electrode, which is consistent with the observed $\text{O}_2^{\bullet-}$ generation during the photocatalysis process. It is known that doping carbon materials with electron-accepting nitrogen atoms can facilitate the oxygen reduction reaction [46,47]. Given C-dots also have electron-accepting ability under light irradiation [21], just like the function of nitrogen atoms, C-dots on rGO may create a net positive charge on the adjacent carbon atoms in rGO nonosheet, which favours the adsorption of oxygen atoms and can readily attract electrons from the anode, thus facilitating the electrochemical oxygen reduction reaction [47]. Fig. 5e shows the photocurrent response of TR and CTR electrodes with solar light irradiation. The photocurrent of CTR is around twice that of TR. It is

widely accepted that the photocurrent is determined mainly by the separation efficiency of the photo-generated electron-hole pairs within the photocatalyst: the higher the photocurrent means the higher the electron-hole separation efficiency [48]. To further study the electron-hole separation efficiency, electrochemical impedance spectroscopy (EIS) was utilized to probe the separation efficiency of charge carrier. As shown by EIS Nyquist plots (Fig. 5f), the arc radius of CTR is smaller than that of TR, indicating lower resistance for CTR electrode [49]. These results further suggest that CTR has a more effective separation of photo-generated electron-hole pairs and a faster interfacial electron transfer than TR.

The above results indicate that the migration of charge-carriers in TR and CTR is different. It is known that the conduction band of TiO_2 is at -0.5 V vs NHE while the Fermi level of rGO is around 0 V vs NHE [12]. Therefore, for graphene based TiO_2 photocatalysts, electrons can transfer from photo-excited TiO_2 to rGO separating electron-hole pairs. In TR nanocomposite, as some TiO_2 particles are aggregated on rGO surface, the electron-hole separation process is inevitably impaired. Moreover, electrons from TiO_2 have to be stored within the C–C networks if there is no additional electron acceptor on rGO surface [12]. Thus, in the TR photocatalytic process, electrons transfer (from photo-excited TiO_2 to rGO and then to O_2 molecule) are hindered, which is not favourable for O_2 reduction (Scheme 2a). With C-dots on rGO surface, electron transfer process for oxygen reduction in CTR nanocomposite is enhanced. Firstly, the well dispersion of TiO_2 on rGO benefits the electron transfer from TiO_2 to rGO, which leads to enhanced electron-hole separation. In addition, C-dots were reported to be good both electron acceptors



Scheme 2. Possible electron transfer paths for O_2 reduction by TR (a) and CTR nanocomposites during photocatalytic water disinfection process.

and donors with light irradiation [21]. As shown in **Scheme 2b**, in CTR photocatalytic process, the electrons from TiO_2 efficiently transfer to C-dots (as electron acceptors) via rGO nanosheet, which acts as a “highway” for shuttling electrons [12,13,50]. Meanwhile, as C-dots are also electron donors and has been used as electrocatalysts for oxygen reduction reaction [22], the trapped electrons in C-dots further donate to O_2 molecules, forming $O_2^{\bullet-}$ radicals. Thus in CTR system, the separation of photo-generated electron-hole pairs is enhanced and the O_2 reduction activity is also boosted simultaneously by the highly dispersed TiO_2 nanocrystals and C-dots.

4. Conclusions

We reported a facile hydrolysis-hydrothermal approach for the synthesis of highly dispersed TiO_2 nanocrystals and C-dots co-decorated rGO sheets. In this strategy, glucose and $TiCl_4$ are precursors and mutual dispersants, respectively, which are critical for forming highly dispersed and uniform-sized C-dots and TiO_2 nanocrystals. Highly dispersed TiO_2 and C-dots promoted the electron transfer from photo-excited TiO_2 and O_2 molecules via conductive rGO sheet, which facilitated the separation of electron-hole pairs as well as the generation of $O_2^{\bullet-}$. In addition, C-dots facilitate the combination of $\bullet OH$ forming H_2O_2 . Due to the longer lifetimes of $O_2^{\bullet-}$ and H_2O_2 , they can diffuse long distance in aqueous solution enhancing the photocatalytic performance on inactivation of *E. coli*. This work could provide a new insight to the development of nanocomposite photocatalysts for environmental application.

Acknowledgements

This study was supported by Australia Research Council (ARC DP140103535). X. Zhang thanks Australian Research Council and Monash University for his ARF (DP110103533) and Larkins fellowships. Dr. Thomas Gengenbach in CSIRO is acknowledged for XPS characterization and data analysis. Dr Qiaoliang Bao and Mr. Jingchao Song in Monash University are acknowledged for Raman characterization. We thank Mr. Bai-Qian Dai in Monash University for his help on TGA analysis. Dr Zheng Xing, Mr. Gen Wang and Ms. Yichun Yin are acknowledged for electrochemical experiments. Ms Shirley Davy-Prefumo and Mr. Manoj Kamalanathan at the School of Biological Sciences, Monash University are thanked for their help on the fluorescence spectrophotometer. The authors acknowledge use of facilities within the Monash Centre for Electron Microscopy (MCEM) and Monash Ramaciotti Centre for Cryo Electron Microscopy.

Appendix A. Supplementary data

Supplementary data associated with this article can be found, in the online version, at <http://dx.doi.org/10.1016/j.apcatb.2016.09.014>.

References

- [1] R.P. Schwarzenbach, B.I. Escher, K. Fenner, T.B. Hofstetter, C.A. Johnson, U. Von Gunten, B. Wehrli, *Science* 313 (2006) 1072–1077.
- [2] Q. Li, S. Mahendra, D.Y. Lyon, L. Brunet, M.V. Liga, D. Li, P.J. Alvarez, *Water Res.* 42 (2008) 4591–4602.
- [3] M.A. Shannon, P.W. Bohn, M. Elimelech, J.G. Georgiadis, B.J. Marinas, A.M. Mayes, *Nature* 452 (2008) 301–310.
- [4] P.-C. Maness, S. Smolinski, D.M. Blake, Z. Huang, E.J. Wolfrum, W.A. Jacoby, *Appl. Environ. Microb.* 65 (1999) 4094–4098.
- [5] C. Wei, W.Y. Lin, Z. Zainal, N.E. Williams, K. Zhu, A.P. Kruizic, R.L. Smith, K. Rajeshwar, *Environ. Sci. Technol.* 28 (1994) 934–938.
- [6] M. Peñalve, N.T. Nolan, S.C. Pillai, M.K. Seery, P. Falaras, A.G. Kontos, P.S. Dunlop, J.W. Hamilton, J.A. Byrne, K. O’shea, *Appl. Catal. B: Environ.* 125 (2012) 331–349.
- [7] H.A. Foster, I.B. Ditta, S. Varghese, A. Steele, *Appl. Microbiol. Biotechnol.* 90 (2011) 1847–1868.
- [8] X. Chen, L. Liu, Y.Y. Peter, S.S. Mao, *Science* 331 (2011) 746–750.
- [9] Q. Xiang, J. Yu, M. Jaroniec, *Chem. Soc. Rev.* 41 (2012) 782–796.
- [10] Q. Huang, S. Tian, D. Zeng, X. Wang, W. Song, Y. Li, W. Xiao, C. Xie, *ACS Catal.* 3 (2013) 1477–1485.
- [11] H. Tong, S. Ouyang, Y. Bi, N. Umezawa, M. Oshikiri, J. Ye, *Adv. Mater.* 24 (2012) 229–251.
- [12] I.V. Lightcap, T.H. Kosel, P.V. Kamat, *Nano Lett.* 10 (2010) 577–583.
- [13] Q. Xiang, J. Yu, M. Jaroniec, *J. Am. Chem. Soc.* 134 (2012) 6575–6578.
- [14] H. Zhang, L.-H. Guo, D. Wang, L. Zhao, B. Wan, *ACS Appl. Mater. Interfaces* 7 (2015) 1816–1823.
- [15] H. Li, Z. Kang, Y. Liu, S.-T. Lee, *J. Mater. Chem.* 22 (2012) 24230–24253.
- [16] S.Y. Lim, W. Shen, Z. Gao, *Chem. Soc. Rev.* 44 (2015) 362–381.
- [17] J. Liu, Y. Liu, N. Liu, Y. Han, X. Zhang, H. Huang, Y. Lifshitz, S.-T. Lee, J. Zhong, Z. Kang, *Science* 347 (2015) 970–974.
- [18] H. Ming, Z. Ma, Y. Liu, K. Pan, H. Yu, F. Wang, Z. Kang, *Dalton Trans.* 41 (2012) 9526–9531.
- [19] S. Zhuo, M. Shao, S.-T. Lee, *ACS Nano* 6 (2012) 1059–1064.
- [20] H. Li, X. He, Z. Kang, H. Huang, Y. Liu, J. Liu, S. Lian, C.H.A. Tsang, X. Yang, S.T. Lee, *Angew. Chem. Int. Ed.* 49 (2010) 4430–4434.
- [21] X. Wang, L. Cao, F. Lu, M.J. Meziani, H. Li, G. Qi, B. Zhou, B.A. Harruff, F. Kermarrec, Y.-P. Sun, *Chem. Commun.* (2009) 3774–3776.
- [22] C. Zhu, J. Zhai, S. Dong, *Chem. Commun.* 48 (2012) 9367–9369.
- [23] W.S. Hummers Jr., R.E. Offeman, *J. Am. Chem. Soc.* 80 (1958), 1339–1339.
- [24] X. Zeng, D.T. McCarthy, A. Deletic, X. Zhang, *Adv. Funct. Mater.* 25 (2015) 4344–4351.
- [25] L. Brunet, D.Y. Lyon, E.M. Hotze, P.J. Alvarez, M.R. Wiesner, *Environ. Sci. Technol.* 43 (2009) 4355–4360.
- [26] A.N. Baga, G.A. Johnson, N.B. Nazhat, R.A. Saadalla-Nazhat, *Anal. Chim. Acta* 204 (1988) 349–353.
- [27] K.-I. Ishibashi, A. Fujishima, T. Watanabe, K. Hashimoto, *Electrochim. Commun.* 2 (2000) 207–210.
- [28] B. Qiu, M. Xing, J. Zhang, *J. Am. Chem. Soc.* 136 (2014) 5852–5855.
- [29] L. Tang, R. Ji, X. Cao, J. Lin, H. Jiang, X. Li, K.S. Teng, C.M. Luk, S. Zeng, J. Hao, *ACS Nano* 6 (2012) 5102–5110.
- [30] Z. Fan, K. Wang, T. Wei, J. Yan, L. Song, B. Shao, *Carbon* 48 (2010) 1686–1689.
- [31] D. He, K. Cheng, T. Peng, M. Pan, S. Mu, *J. Mater. Chem. A* 1 (2013) 2126–2132.

[32] S. Sahu, B. Behera, T.K. Maiti, S. Mohapatra, *Chem. Commun.* 48 (2012) 8835–8837.

[33] O. Akhavan, M. Abdolahad, A. Esfandiar, M. Mohatashamifar, *J. Phys. Chem. C* 114 (2010) 12955–12959.

[34] D. Graf, F. Molitor, K. Ensslin, C. Stampfer, A. Jungen, C. Hierold, L. Wirtz, *Nano Lett.* 7 (2007) 238–242.

[35] B.J. Moon, Y. Oh, D.H. Shin, S.J. Kim, S.H. Lee, T.-W. Kim, M. Park, S. Bae, *Chem. Mater.* 28 (2016) 1481–1488.

[36] M.Y. Xing, D.Y. Qi, J.L. Zhang, F. Chen, *Chem. Eur. J.* 17 (2011) 11432–11436.

[37] Z.-C. Yang, M. Wang, A.M. Yong, S.Y. Wong, X.-H. Zhang, H. Tan, A.Y. Chang, X. Li, J. Wang, *Chem. Commun.* 47 (2011) 11615–11617.

[38] H. Peng, J. Travas-Sejdic, *Chem. Mater.* 21 (2009) 5563–5565.

[39] W.-R. Li, X.-B. Xie, Q.-S. Shi, H.-Y. Zeng, O.-Y. You-Sheng, Y.-B. Chen, *Appl. Microbiol. Biotechnol.* 85 (2010) 1115–1122.

[40] S. Liu, T.H. Zeng, M. Hofmann, E. Burcombe, J. Wei, R. Jiang, J. Kong, Y. Chen, *ACS Nano* 5 (2011) 6971–6980.

[41] W. Wang, Y. Yu, T. An, G. Li, H.Y. Yip, J.C. Yu, P.K. Wong, *Environ. Sci. Technol.* 46 (2012) 4599–4606.

[42] H. Sheng, H. Ji, W. Ma, C. Chen, J. Zhao, *Angew. Chem.* 125 (2013) 9868–9872.

[43] G.-h. Moon, W. Kim, A.D. Bokare, N.-e. Sung, W. Choi, *Energy Environ. Sci.* 7 (2014) 4023–4028.

[44] R.W. Redmond, I.E. Kochevar, *Photochem. Photobiol.* 82 (2006) 1178–1186.

[45] N.M. Dimitrijevic, E. Rozhkova, T. Rajh, *J. Am. Chem. Soc.* 131 (2009) 2893–2899.

[46] K. Gong, F. Du, Z. Xia, M. Durstock, L. Dai, *Science* 323 (2009) 760–764.

[47] S. Yang, X. Feng, X. Wang, K. Müllen, *Angew. Chem. Int. Ed.* 50 (2011) 5339–5343.

[48] M. Kong, Y. Li, X. Chen, T. Tian, P. Fang, F. Zheng, X. Zhao, *J. Am. Chem. Soc.* 133 (2011) 16414–16417.

[49] M. Adachi, M. Sakamoto, J. Jiu, Y. Ogata, S. Isoda, *J. Phys. Chem. B* 110 (2006) 13872–13880.

[50] K. Iwashina, A. Iwase, Y.H. Ng, R. Amal, A. Kudo, *J. Am. Chem. Soc.* 137 (2015) 604–607.